

Latest Edition

Welcome to the IEDM 2013 edition of the TCAD News. Although there are still a few weeks before we close the year, IC sales in 2013 is shaping up to be all-time high if the 6% growth from 2012 (forecasted by most analysts) holds up. As we gather in Washington, D.C. to learn about the latest advances in semiconductor technology development, we can look back at 2013 as a testament to the ingenuity and drive of the IC industry. Computing and storage applications can now be serviced with 16/14nm FinFET and 3D-NAND technologies, and in both of these segments the research and development for the next generation is well underway. The critical role of power device technologies in fostering energy efficient systems, ranging from power management in mobile platforms to converters for electric and hybrid vehicles, provides strong impetus to the continuous development of silicon-based and wide-bandgap power devices.

As the industry begins exploring sub-10nm devices, at SISPAD 2013, TSMC¹ and Intel² presentations highlighted the value of TCAD for continued scaling. Encouraged by these validations, I am pleased to announce the availability of the Sentaurus I-2013.12 release with over 120 enhancements to support the development of semiconductor technologies for logic, memory, analog, power and optoelectronic applications. I trust that you will find these enhancements in the I-2013.12 to be helpful in the development of next generation devices.

With the approaching holiday season, I would also like to take this opportunity to wish you happy holidays and a prosperous New Year.

With warm regards,

Terry Ma
Vice President of Engineering, TCAD

Contact TCAD

For further information and inquiries:
tcad_team@synopsys.com

TCAD news

Overview of Sentaurus I-2013.12

In keeping with recent releases, we continue with the focus on enhancing 3D capabilities for modeling FinFETs, 3D memory, power devices and CMOS image sensors. Variability analysis with the impedance field method (IFM) has proven to be a computationally efficient way for analyzing device variability, and we continue to increase its functionality covering a wider range of random fluctuations in devices. Our support for new materials for logic applications has been further enhanced with updated models for SiGe, Ge, and III-V materials. A number of new features address the fast rising interest in SiC and GaN development: these include the introduction of SiC oxidation, a more realistic ohmic boundary condition, and numerous numerics improvements. Updated mechanics models have been added to Sentaurus Interconnect to address a widening range of BEOL reliability and TSV applications. In the area of image sensors, we added a number of enhancements to the EMW solver and improved the MPI parallelization efficiency by 1.5X.

Sentaurus Process

Improved Electrostatics Modeling

Previously, the electrical potential in Sentaurus Process was only calculated in bulk semiconductor materials. Starting with release I-2013.12, the Poisson equation can now be solved in insulators, at metal interfaces, and hetero-interfaces such as Si/SiGe. This feature improves the simulation

accuracy of dopant diffusion and segregation near material interfaces. Poisson's equation is given by,

$$\nabla \cdot (\epsilon_r \epsilon_0 \nabla(\psi - \theta)) = -q(p - n + \Delta N)$$

$$q\theta = \chi + \frac{E_g}{2} + \frac{kT}{2} \ln\left(\frac{N_c}{N_v}\right)$$

$$n = n_i \exp\left(\frac{q\psi}{kT}\right), \quad p = n_i \exp\left(-\frac{q\psi}{kT}\right)$$

$$n_i = \sqrt{N_c N_v} \exp\left(-\frac{E_g}{2kT}\right)$$

where χ , E_g , N_c and N_v are the affinity, energy bandgap, density of states of conduction and valence bands respectively, which depend on mole-fraction as well as material properties. At interfaces, the Dirichlet boundary condition is automatically applied at metal/insulator or metal/semiconductor interfaces while a continuous boundary condition is applied at other interfaces. By default, the work functions are set for the following conductors; Aluminum, Cobalt, CobaltSilicide, Copper, Metal, Nickel, Platinum, TiNitride, TiSilicide, Titanium, Tungsten, and TungstenSilicide.

Diffusion, Activation and Oxidation in SiC

By default, the Constant model for diffusion and the Solid model for activation are set for aluminum, boron, nitrogen and phosphorus. Carbon atoms are generated during SiC oxidation. Some of carbon atoms diffuse into the oxide and react with diffusing oxidants. The reaction of carbon atoms with oxygen atoms generates carbon-oxide compounds. Since CO₂ formation requires

¹J. Wu and C. Diaz, "Expanding Role of Predictive TCAD in Advanced Technology Development," Proc. SISPAD 2013, pp. 167-171.

²C. Weber et. al., "Technology CAD Challenges of Modeling Multi-gate Transistors," Proc. SISPAD 2013, pp. 117-118.



higher energy than CO formation, only CO, which is assumed to be instantly evaporated, is accounted for. Some of carbon atoms are captured at oxidizing interfaces and reduce the oxidant reaction rate. Although silicon atoms also are generated and diffuse into the oxide, it is assumed that the Si-O reaction occurs primarily at the SiC/oxide interface because Si diffusivity in oxide is very low. Thus, a 2-stream diffusion model is used, accounting for carbon and oxidant diffusion in oxide.

$$\frac{\partial C_{ox}}{\partial t} = \nabla(D_{ox}\nabla C_{ox}) - k_b C_C \frac{C_{ox}}{C_{ox}^0}$$

$$\frac{\partial C_C}{\partial t} = \nabla(D_C\nabla C_C) - k_b C_C \frac{C_{ox}}{C_{ox}^0}$$

$$\frac{\partial \sigma_C}{\partial t} = t(\sigma_{C,max} - \sigma_C)C_C - eC_{C,max}\sigma_C$$

Carbon atoms which diffuse to an oxide surface evaporate at a given rate. At SiC/oxide interfaces, the incoming flux of oxidants and carbon atoms into oxide are modeled by:

$$F_{ox} = -k_i \left(1 - \frac{\sigma_C}{\sigma_{C,max}}\right) C_{ox}$$

$$F_C = r_C F_{ox} - \frac{\partial \sigma_C}{\partial t}$$

Default parameters are provided for the Si-face (0001) and C-face (000 $\bar{1}$), in both O₂ and H₂O ambients and for (11 $\bar{2}$ 0) in O₂. The model parameters are calibrated with measured data[1][2]. The generation and diffusion of point-defects during oxidation, carbon and silicon interstitials and vacancies, can also be simulated.

Improved Implant Boundary Conditions

In ion implantation, boundary conditions are needed in order to account for geometric effects (such as shadowing) and lateral scattering due to the structural details outside the simulation domain. Simulation of these effects requires knowledge of the materials and damage concentration outside the simulation domain. This information is synthesized by the definition of the implant boundary conditions.

Originally **Periodic** and **Reflect** boundary conditions were developed based on the assumption that the devices are isolated. Therefore, the **Periodic** boundary condition was implemented as follows (refer to Figure 1):

- ▶ The ion beam starts slightly above the top of the structure, that is, the height from surface of structure is very small, but is finite
- ▶ The window width of the ion beam may be larger or smaller than the simulation domain but the left and right positions of the beam are chosen such that the ion beam covers the whole surface (shadowing will be taken into account)

In this implementation, boundaries exist only in solid regions, and when a particle reaches one side of boundary it will be moved to the other side of the boundary. However, in ambient (or Gas), particles are free to enter or exit. Therefore, the periodic boundary condition, as implemented in Sentaurus Process, simply means translating the position of particles from one boundary to the opposite boundary in solid regions. It takes the structure as is, and does not extend to form a true periodic structure. The simulation domain needs to be carefully chosen in order for this boundary condition to be valid.

This boundary condition works fine if there is only one device (e.g., a well isolated device), and the boundaries are free from shadowing from neighboring devices. For an array of closely packed devices, this boundary condition may give inaccurate results, as geometric and lateral scattering effects due to neighboring devices are not taken into account. One potential inaccurate result is incorrect shadowing as shown in Figure 2. Another possible result is loss of dose in silicon regions, as shown in Figure 3.

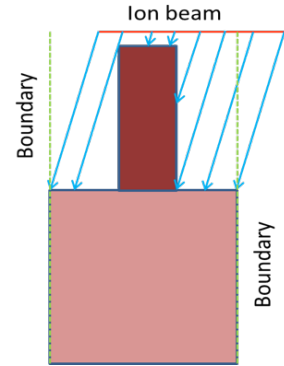


Figure 1: Illustration of how particles are launched in MC implantation with older simplified periodic boundary condition.

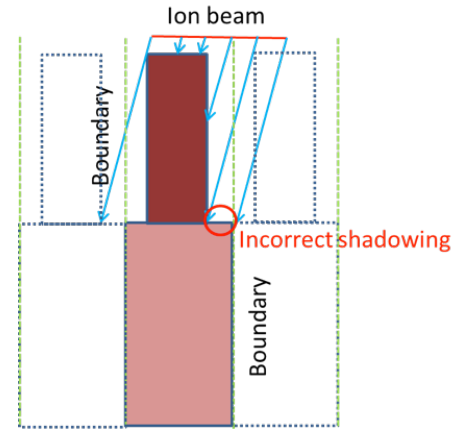


Figure 2: Shadowing by neighboring device not taken into account in older simplified periodic boundary condition.

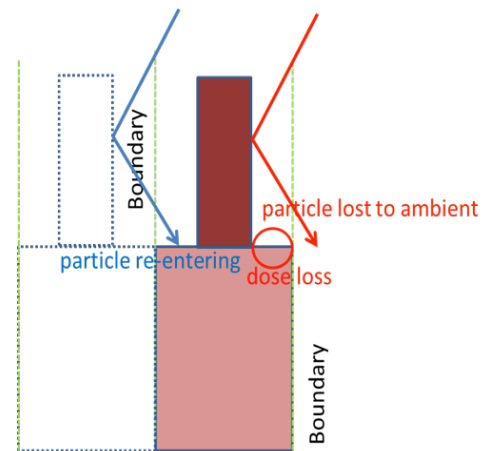


Figure 3: Dose loss to ambient in older simplified Periodic boundary condition.



In order to improve the accuracy for periodic structures, we have implemented **TruePeriodic** boundary conditions. This implementation incorporates two main differences relative to the older simplified periodic boundary conditions (Figure 4):

- ▶ Particles are launched from within the domain
- ▶ Particles are also translated in Gas boundary. Therefore, when a particle hits the Gas boundary, it will also be moved to the other side of the boundary, just like in solid regions

With this implementation, the shadowing effect by neighboring devices is explicitly taken into account without expanding the simulation domain. In addition, the dose loss in the older simplified periodic boundary condition is also improved (refer to Figure 5).

For simplicity, we have only shown 2D figures. The implementation in 3D is much more complicated, but the same principle applies.

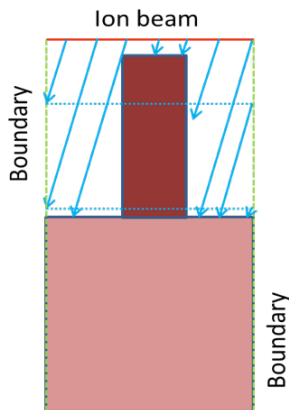


Figure 4: Schematic for correct periodic boundary condition, i.e., **TruePeriodic** boundary condition.

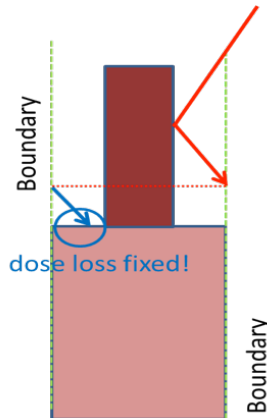


Figure 5: Treatment of dose loss in **TruePeriodic** boundary condition.

Similar to the **Periodic** boundary condition, the **Reflect** boundary condition also works for single devices. In the **Reflect** boundary condition, similar to the **Periodic** boundary condition, the ion beam is launched from just above the device and covers the whole surface. However, in contrast to the **Periodic** BC, when ions exit the boundary, the direction of the ion is reflected with respect to the boundary instead of moving the ion from one side of the boundary to the opposite side of the boundary. Unfortunately for the **Reflect** boundary condition, since the ion beam does not have reflective symmetry, such reflection of ion directions breaks the symmetry, thus causing inaccurate results in most implant conditions. Therefore, this **Reflect** boundary condition is only applicable for tilt=0 implants.

In order to overcome this problem, we have devised a **TrueReflect** boundary condition. When an array of devices has reflective symmetry, it also has periodic symmetry with a period doubling that of the domain size (Figure 6). In such cases, we can “smartly” convert the reflective boundary condition problem into a periodic boundary condition problem and ensure that the simulation results are correct under all implant conditions.

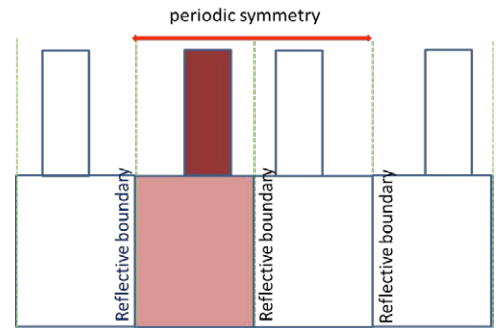


Figure 6: Illustration of how **Reflect** boundary condition can be converted into periodic boundary condition by using larger simulation domain.

Due to a larger simulation domain used in **TrueReflect** boundary condition, the simulation time is generally longer. However, if the ion beam has reflective symmetry (such as tilt=0 or approximately multi-rotation implant), Sentaurus Process allows the average of the implant profiles over the original and reflected domains. Therefore, none of the simulated particles are wasted, and there is very little performance penalty in **TrueReflect** over the simplified **Reflect** boundary conditions.

Therefore, for improved accuracy, **TruePeriodic** or **TrueReflect** boundary conditions are always recommended over the simplified **Periodic** or **Reflect** boundary conditions when simulating an array of devices or a half or quarter cell of devices with trenches.

Unified Implant Boundary Conditions

There are currently two sets of implant boundary conditions: one for analytic implant (under directory **ImplantData**), and another for MC implant (under directory **MCImplant**). This arrangement has the advantage that the boundary conditions for analytic or MC implant can be specified separately and thus tailored to the particular implant scenario. However, most users wish to use the same set of boundary conditions in order to get more consistent results in analytic and MC



implant. In addition, the current `Periodic BC` has higher precedence over other types of boundary conditions. Thus, if `Periodic` or `TruePeriodic BC` is `True`, it has to be disabled before other types of boundary conditions can be specified. In order to solve these issues, we provide a new unified method for specifying implant boundary conditions.

In this scheme, instead of using PDB commands to specify the implant boundary conditions, we use the `implant` command to specify the boundary conditions with the following syntax:

```
implant boundary.conditions =  
{left=<c> right=<c> front=<c>  
back=<c>}
```

where the valid keywords are `Periodic`, `Reflect`, or `Extend`.

In contrast to the boundary conditions specified by PDB, here if `Periodic` or `Reflect` is specified in the `implant` command, `TruePeriodic` and `TrueReflect` will be used in MC implant. This is because `TruePeriodic` and `TrueReflect` in MC implant are equivalent to `Periodic` and `Reflect` in analytic implant, respectively, thus ensuring the most consistent results between analytic and MC implants.

For simplicity, users don't need to specify boundary conditions for all sides. Default `Extend BC` is assumed for unspecified sides, except for periodic BC. Since periodic boundary conditions need to be paired, left and right, or front and back, the same BC must be applied to both sides. Users are allowed to specify periodic BC on one side. If the other side is specified with a different type of BC, a warning is issued, and periodic BC is assumed.

This new scheme provides full backward compatibility, and is the recommended method for specifying implant boundary conditions when creating new input files.

Advanced Calibration for Power Devices

For power devices, process simulation is often time consuming because many mesh points are needed and because a high number of thermal anneals and oxidations are used in the fabrication process. For many types of power devices, from the simulation perspective, the process simulation consists of two parts:

- ▶ In the first part of process simulation, the concentration of dopants is small and the thermal budget for annealing and oxidation steps is large. Most of the CPU time is needed in this part
- ▶ In the second part, typically related to contact formation, the maximum dopant concentration is high, and the thermal budget for thermal annealing after implantation is small

For these devices, the CPU time for process simulation can be reduced without loss of accuracy by using simpler models and faster settings in the first part of the process simulation and switching to standard Advanced Calibration models for the second part of the process simulation, where transient enhanced diffusion after implantation and dopant clustering play a significant role.

For convenient use of this speed up concept, new procedures `AdvancedPowerDeviceMode` and `AdvancedPowerDeviceModeReset` have been defined in the Advanced Calibration file for Sentaurus Process. They allow turning on and off in a single command line a selection of simplified models settings which have been tested and optimized for a wide range of power device processes. The use of these procedures reduces the total process simulation time by typically 20% - 60%.

Advanced Calibration: Improved Accuracy for Arsenic and Phosphorus Diffusion in Silicon

In the frame of the European research project *Atemox*, Synopsys has completed a comprehensive revision of diffusivities of As and P in silicon. As and P diffuse via dopant defect pairs, which may form in various charge states. In the case of As-V pairs these are: As^+V^0 , As^+V^- , As^+V^{2-} .

The focus of the analysis was to determine the relative contributions of pairs in different charge states to the total diffusivity of As and P. The charge state distribution governs (a) the dependency of pair diffusivity on the local electron concentration and (b) the drift of dopant-defect pairs in regions of strong electric fields. As the main result of the analysis, the relative contribution of P^+I^0 pairs to P diffusion was increased and the relative contribution of P^+I^- pairs was decreased. This improves the out-of-the-box accuracy, most significantly for the simulation for As^+P co-diffusion, where the electric field across steep As profiles causes a hump in annealed P profiles, sensitive to the charge states distribution of P-I pairs. For As, the diffusivity of As via As^+V^- pairs, responsible for the "box-shape" of As profiles, was increased.

The improved values for pair diffusion of P-I, P-V, As-I, and As-V pairs in various charge states have been calibrated against SIMS data for many process conditions, extensively tested in 1D and 2D process simulation and integrated in the Advanced Calibration file for continuum Sentaurus Process, Release I-2013.12.

In addition, a recalibration of As and P in silicon has also been included in the Advanced Calibration file for Sentaurus Process Kinetic Monte Carlo of Release I-2013.12. The As-I and As-V diffusivities are now based on Martin-Bragado et al. [3], which are not the same but are similar to continuum Advanced Calibration Version I-2013.12. The increased As diffusivity in

heavily-doped n-type silicon is modeled by mobile As^V and As^{PV} clusters, in close agreement to the experimental observations and quite similar to the percolation diffusion model. To further improve the accuracy for low anneal temperatures, for instance for heated implantation, As-I diffusivity at low temperature got enhanced. The As deactivation by As clusters has also been revised. Larger As-I clusters have been added with energies based on ab initio data [4], again to improve the accuracy for low anneal temperatures. P deactivation at very high concentrations is now enhanced by inclusion of the percolation deactivation effect. In a percolation event, P can react with single or clustered P in its neighborhood without migration. This provides an additional mechanism for dopant deactivation at high concentrations beyond the standard diffusion-limited dopant defect clustering. In addition, the P-V pair diffusivity prefactors, the P-I binding energy, and the P dose loss at the Si/SiO₂ interfaces have been adjusted.

Other models, which have been improved or added in the Advanced Calibration file for Sentaurus Process, Release I-2013.12 include:

- ▶ Calibration for diffusion and dopant activation during epitaxial growth of silicon
- ▶ Calibration for melt laser anneal
- ▶ Model revised for N diffusion and clustering in silicon
- ▶ Oxidation enhanced diffusion under n+-doped silicon surfaces
- ▶ Calibration of B activation in Ge substrates

A complete list with detailed documentation of all items is presented in the Release Notes.

GDSII File Reading Capability

For several releases, ICWB-EV+ has been used to define masks for Sentaurus Process. With this release it is now also possible to read GDSII files directly into Sentaurus Process to generate masks for layout-driven simulations. The GDSII file can be at any level of integration in the hierarchy: full chip, test chip, or a single cell, while users have the option to define a specific simulation domain from the layout file. The simulation domain

can be 2D or 3D, where a 2D domain is defined by two endpoints of a segment and a 3D domain is defined by two opposite corners of the simulation domain. There are also options to scale and stretch the selected domain. The new option provides an entirely script-based interface to GDSII. However, to determine the exact location of the desired simulation domain, a GDSII viewer, such as ICWB-EV+, is still useful.

3D Oxidation Improvements

To control the smoothness of material interfaces, the new parameter **Remove.Dist.On.Interface** has been introduced. An interface triangle with an edge shorter than this distance will be removed. A smaller threshold will make the interfaces smoother but will increase the number of triangles. Figure 7 shows the effect of this parameter. For clarity, the grown oxide is shown in outline.

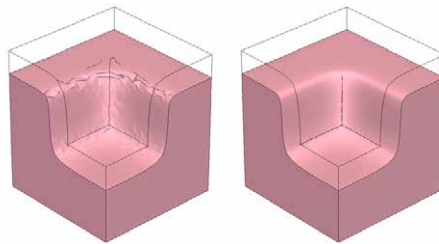


Figure 7: Smoothness of the oxidizing interface is controlled by the new parameter `Remove.Dist.On.Interface`.

Figure 8 shows the oxidant concentration of the LOCOS oxidation with a 115nm nitride mask corner. The temperature is ramped up from 800C to 950C at a rate 10C/min, stays at 950C for 655min, and is ramped down to 800C at the rate -3C/min. During the 720min oxidation, the composition of O₂, N₂, H₂ varies over time: 0.5l/min O₂ + 10l/min N₂ for 25min, 6.5l/min O₂ for 5min, 3.5l/min O₂ + 3l/min H₂ for 5s, 6.5l/min O₂ + 6l/min H₂ for 630min, 0.5l/min O₂ + 10l/min N₂ for 60min. The grown oxide thickness varies from 10nm to 1010nm. The simulation time is 887min on an AMD Opteron 2.7GHz computer with 32GB RAM.

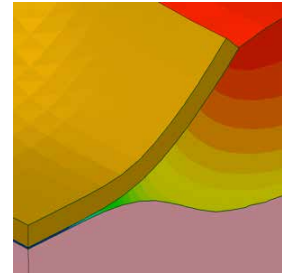


Figure 8: Oxidant concentration after LOCOS oxidation of a mask corner.

Figure 9 shows the oxidant concentration after a trench oxidation, a gate oxidation, and a poly re-oxidation. For clarity, the polysilicon is shown in outline. The trench oxidation happens at 1050C with 1l/min H₂ + 2l/min O₂ + 8l/min N₂ for 10min. The gate oxidation happens at 1000C with 1l/min O₂ for 20min. The poly re-oxidation happens at 950C with 0.5l/min O₂ + 9.5l/min N₂ for 7min. The simulation time for the trench oxidation, the gate oxidation, and the poly re-oxidation is 342min, 258min, and 28min, respectively, on an Intel Xeon 2.6GHz computer with 258GB RAM.

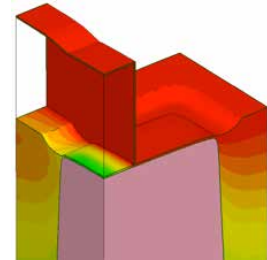


Figure 9: Oxidant concentration after a process flow that includes a trench oxidation, a gate oxidation, and a poly re-oxidation.

3D Trapezoidal Deposition

Three-dimensional diamond and rhomboid shapes are now easily created using trapezoidal deposition. Through the definition of wall height and wall angle, Sentaurus Process generates the shape of the given deposition material in 3D, deposited selectively on a user-defined set of material surfaces.

The wall angle is measured in degrees from horizontal, where 90° is vertical; angles greater than ninety degrees spread outward as height increases, and angles less than ninety degrees close inward with increasing height.



Separate outward and inward deposition steps can be used to create diamond-like shapes, as shown in Figure 10.

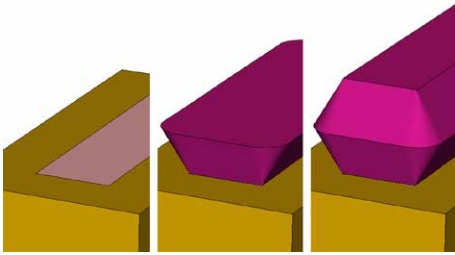


Figure 10: (Left) Initial structure surface with exposed Silicon masked laterally by Silicon Nitride, (Center) first deposition step of PolySilicon on Silicon with wall angle equal to 120 degrees, (Right) second deposition step, PolySilicon on PolySilicon, with wall angle equal to 60 degrees.

Automatic Parameter Optimization

In previous releases, users had to rely on the optimizer in Sentaurus Workbench to perform parameter optimization. In this release, Sentaurus Process provides a built-in capability for parameter optimization. To use this feature, a Tcl procedure must be created which takes as input the current values of the parameters to be optimized, and returns a corresponding result. Though writing the procedure is a small extra task for the user, this design allows for great flexibility in the types of optimization that can be performed. The procedure can specify anything from a simple analytic function to a complete process simulation flow. Similarly the form of the result is simply a vector of values from which an error is computed based on the user's target data. This generic flow allows for a wide variety of applications, for example dopant profiles resulting from multiple process steps, or the thickness of an oxide layer.

Sentaurus Interconnect

Fracture Mechanics Enhancements

Several enhancements have been implemented in I-2013.12 for J integral calculation, crack definition and cohesive zone material modeling.

C(t) Integral for Viscoplastic Material

The C(t) integral is used to characterize the amplitude of stresses around crack tips in viscoplastic materials [5][6][7]. The C(t) integral is obtained by replacing strains with strain rates and displacements with velocities in the expression for the J integral. Immediately after loading the crack, the C(t) integral is path dependent: it has a large value near the crack tip but its value drops away from the crack tip. At longer times after loading, as stresses and strain around the crack tip reach a steady value, the C(t) integral becomes path independent: it has much smaller variation with time and distance from the crack tip.

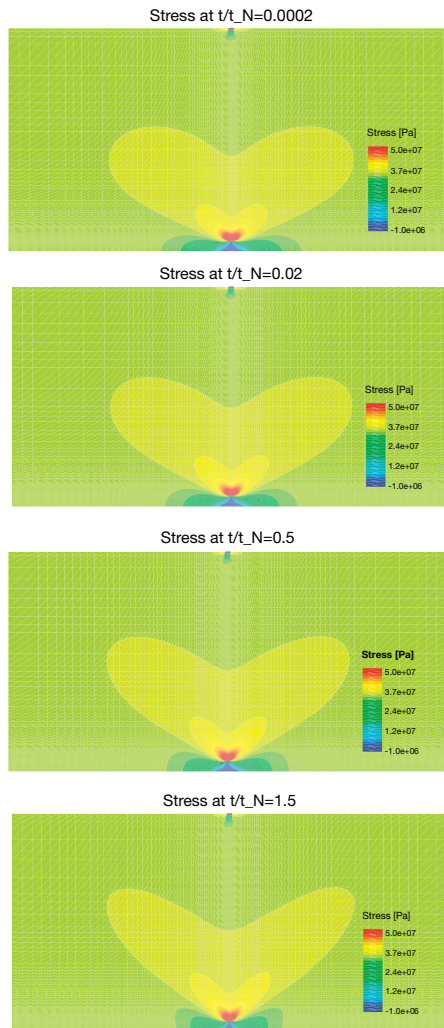


Figure 11: Variation of Stress-YY in shallow edge crack plate over time.

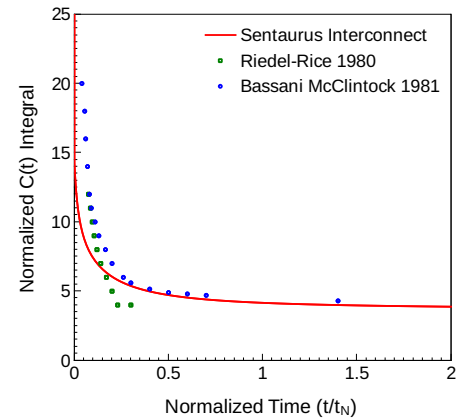


Figure 12: Comparison of variation of C(t) integral with time with reference solution.

To demonstrate the capability, we consider a shallow edge crack in a rectangular plate under plane strain as described in [6]. The crack length to plate width ratio is

$$\frac{a}{W} = \frac{1}{21}$$

A tensile stress normal to the crack, $\sigma_N = E/2000$, where $E = 6.9 \times 10^{11}$ dyn/cm² is the Young's modulus, is applied on opposite ends of the plate. Using the Power Law Creep material model, $\dot{\epsilon}^r = 2.435 \times 10^{-29} \bar{\sigma}^3$, where $\dot{\epsilon}^r$ is the creep strain rate and $\bar{\sigma}$ is the von-Mises stress in dyn/cm², and a Poisson ratio $\nu = 0.3$, we compute stresses and the C(t) integral over time. Figure 11 shows the stress evolution around the crack over time. Figure 12 shows the variation of the normalized C(t) integral

$$\left(\frac{C(t)}{\sigma_N \dot{\epsilon}_N^{cI} a} \right),$$

with normalized time

$$\left(\frac{t}{t_N} \right)$$

where t_N is a relaxation time

$$t_N = \frac{\epsilon_N^{cI}}{\dot{\epsilon}_N^{cI}} = \frac{\sigma_N / E}{2.435 \times 10^{-29} (\sigma_N)^3} = 0.5 \text{ s.}$$

The results are also compared with reference solutions given in [5] and [6].



J_v Integral for Viscoelastic Material

For a crack in viscoelastic material, stresses and strains in the region ahead of the crack tip change over time. J_v integral provides a way to compute the J integral value around a crack tip using stresses and strains in a reference elastic body based on the correspondence principle [7][8].

As an example, J_v integral calculations are performed for a center cracked tension (CCT) rectangular plate with crack length to plate width ratio of

$$\frac{a}{W} = 0.2$$

and a tensile stress $\sigma_N=100$ MPa applied normal to the crack on opposite ends of the plate. The crack is modeled as a bulk crack with Maxwell viscoelastic material model. Material properties for the Maxwell model are: $K=33$ GPa, $G=28.2$ GPa,

$$\tau = \frac{\eta_K}{K} = \frac{\eta_G}{G} = 0.5 \text{ s.}$$

Although a constant tensile stress is applied to the plate at the beginning of the analysis, creep causes stresses and strains to change with time. Figure 13 shows stresses and creep strains a long time after loading the cracked plate. Figure 14 shows the variation of J and J_v integral (normalized with J integral value immediately after loading) over time. The large increase in the value of J integral clearly shows that it is not suitable for viscoelastic materials.

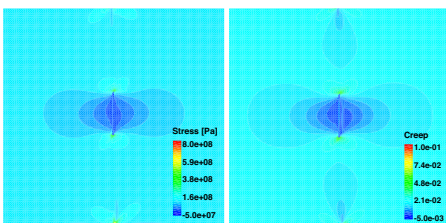


Figure 13: Stress-YY (left) and CreepStrain-YY (right) at for $\frac{t}{\tau}=12$ Maxwell model.

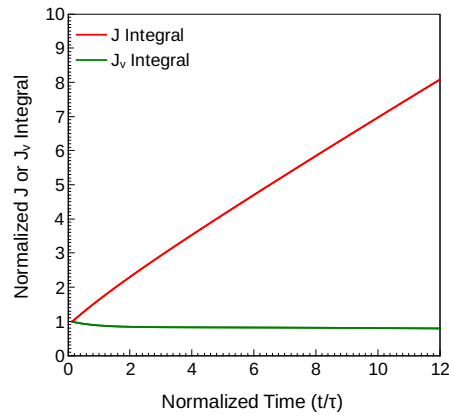


Figure 14: Variation of J and J_v integral with time for Maxwell model.

Partially Open Cracks

The **Crack** command has been enhanced to allow the specification of the cohesive zone material (CZM) model over part of the crack. New parameters have been added to define the parts of the crack with (initially closed) or without (initially open) CZM. The default behavior of entire crack surface being initially open when CZM is not specified, and being initially closed when CZM is specified, remains unchanged.

Figure 15 and Figure 16 show the deformed shape of structures with initially partially open cracks. The cracks propagate as the initially closed parts separate under applied loads (displacements or temperature ramps).

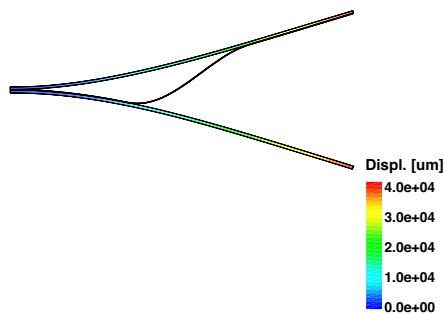


Figure 15: Deformed shape of a double cantilever beam with two partially open cracks. The color indicates the amount of displacement.

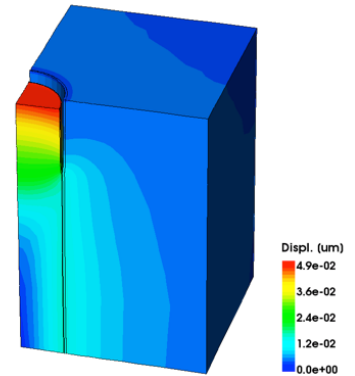


Figure 16: Quarter symmetry model of delamination of TSV from liner. The color indicates the amount of displacement.

Bulk Cracks

Cracks can now be defined within bulk material. In 2D, bulk cracks can be defined using one or more line segments specified in terms of point coordinates. Multiple line segments define a segmented crack curve. In 3D, bulk cracks can be defined using one or more previously specified polygons. Multiple polygons define a faceted crack surface. Figure 17 shows a 3D block with a penny-shaped crack that deforms into a bubble.

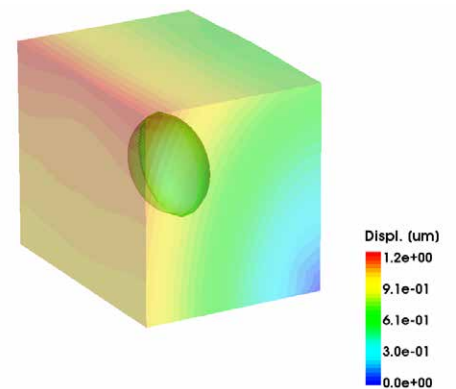


Figure 17: Deformed shape of a penny-shaped crack embedded in a 3D block. The color indicates the amount of displacement.



V-notch Cracks

Cracks can now be defined for V-notches. To define such a crack, the V-notch region is filled with Gas material and an interface crack is defined with one of the materials being Gas. The notch is identified by picking the smallest angle between two adjacent edges in 2D and two adjacent faces in 3D along the crack surface.

Second Order Elements

Second order triangles and tetrahedrons can now be used for defining cracks. These elements can also be used for stress analysis with the cohesive zone material (CZM) model. The calculation of cohesive traction and separation correctly accounts for the higher order interpolation of the underlying mesh elements. J integral calculations (including C(t) integral and J_v integral) have also been enhanced to use the data fields for second order elements when such elements are requested for stress analysis or postprocessing.

Standard Linear Solid Model

In this release, a new viscoelastic material model has been added. The Standard Linear Solid (SLS) model combines elastic response in parallel with a Maxwell model based viscoelastic response as shown in Figure 18. In comparison to Maxwell model, the new model allows stresses to relax to a non-zero value that depends on the bulk and shear moduli of the parallel elastic element.

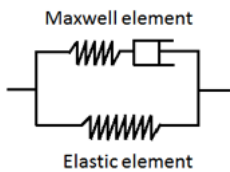


Figure 18: Standard Linear Solid model.

The elastic response is inactive, by default, so that the material behavior is similar to that of the Maxwell model. The elastic response can be activated by specifying non-zero values of bulk and shear moduli.

To illustrate the difference between the Standard Linear Solid model (with non-zero elastic response) and the Maxwell model, we compare results for stress relaxation and creep tests in Figure 19 and Figure 20, respectively.

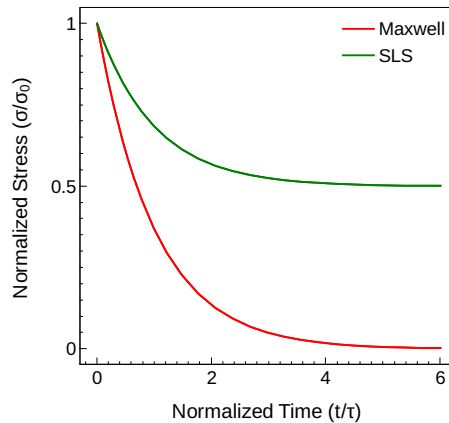


Figure 19: Variation of stress with time for relaxation test with SLS and Maxwell models.

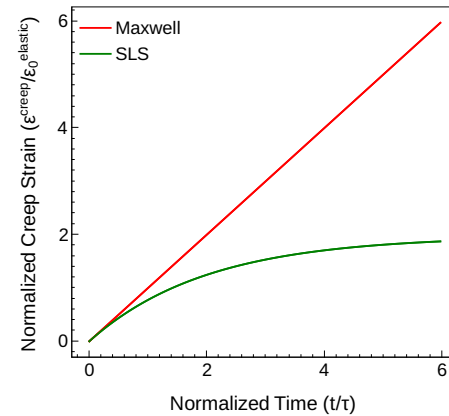


Figure 20: Variation of creep strain with time for creep test with SLS and Maxwell models.

Standard Linear Solid model also allows viscosity to be dependent on temperature and stress (Eyring model:

$$\eta(\bar{\sigma}, T) = \eta(T) \frac{\bar{\sigma}/\sigma_{crit}}{\sinh(\bar{\sigma}/\sigma_{crit})}$$

An implicit non-linear solution scheme based on Newton-Raphson iterations is used for stress solution. Figure 21 shows comparison of stresses for a relaxation test with constant temperature and stress dependent viscosity. The results for nonlinear viscosity are consistent with expected behavior – higher initial stress causes lower viscosity and faster relaxation that slows down at lower stress due to higher viscosity.

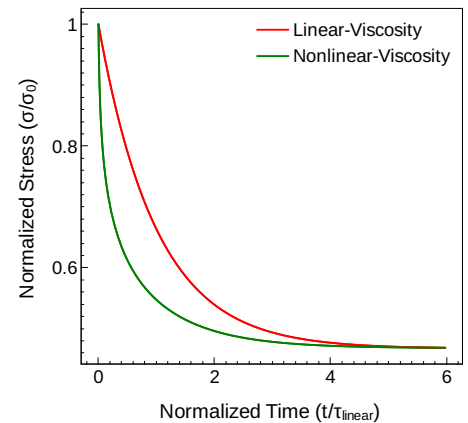


Figure 21: Variation of stress with time for relaxation test with linear and nonlinear viscosity.

Sentaurus Topography 3D Simulation of Tilted and Rotating Wafers for Step Coverage Optimization

Sentaurus Topography 3D can now model topography processing on wafers that are rotated around an axis orthogonal to the substrate and tilted with respect to the vertical direction of the reactor, as shown in Figure 22.

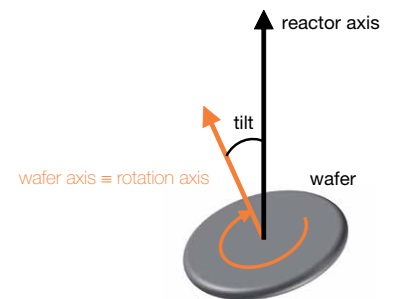


Figure 22: Tilted and rotating wafer.



This feature is available for rate formula module (RFM) models, and it is enabled by setting `rotation=continuous` in the `define_deposit_machine` and `define_etch_machine` commands [9].

Assuming that the wafer rotation period is much smaller than the process time, etching and deposition rates are computed by averaging the number of particles reaching the surface per unit time and area over a rotation period. Therefore, the process time does not need to be split into time intervals of constant wafer angular position, and topography processes on tilted and rotating wafers can be simulated without performance penalty.

This new feature is used here to simulate physical vapor deposition (PVD) processes where wafers are mounted on a planetary system. As described in [10], proper selection of the tilt angle improves the step coverage obtained using this setup.

An RFM model for a PVD process, where the deposition rate is assumed to be proportional to the incoming flux of particles P , can be defined as follows:

```
define_model model=RFM_PVD type=deposit
description="Physical Vapor Deposition model"
add_ion_flux model=RFM_PVD name=P reflection=off sputtering=off
energy=independent
add_float_parameter model=RFM_PVD name=rate quantity=velocity scope=global
add_formula model=RFM_PVD expression="rate()*direct_flux(P)"
finalize_model model=RFM_PVD
```

The `RFM_PVD` model can then be used to define a deposition machine for a tilted and rotating wafer, after specifying the angular distribution `pvd_iad` of the involved particles P :

```
define_iad name=pvd_iad species=P exponent=10000
define_deposit_
```

```
machine model=RFM_PVD
material=Aluminum iad=pvd_iad
rate=1 \
tilt=... rotation=continuous
```

The above-defined deposition machine is used to compute the step coverage for trenches of different aspect ratios on a rotating wafer when using different tilt angles. The step coverage is measured by the following parameter:

$$S_c = \frac{D_{sw}}{|D_b - D_{sw}|}$$

where D_{sw} and D_b denote the average thickness of the deposited layer on the sidewall and on the bottom, respectively. When good step coverage is obtained, then $D_{sw} \approx D_b$ and S_c becomes large. On the other hand, it can be easily shown that $S_c \lesssim 1$, when $D_{sw} \ll D_b$ or $D_{sw} \gg D_b$, that is, when the step coverage is poor.

The values of the D_{sw} and D parameters can be extracted using the `extract` command of Sentaurus Topography 3D with `type=interface`, which allows you to obtain the position of the interfaces between any pair of materials of the simulated structure [9].

In Figure 23, the values of S_c for trenches of different aspect ratio are plotted as a function of the wafer tilt angle. The reported plots clearly show that, for each aspect ratio, there is a tilt angle value that provides the best step coverage. Moreover, as observed in [10], such an optimal value of the tilt angle decreases as the trench aspect ratio increases.

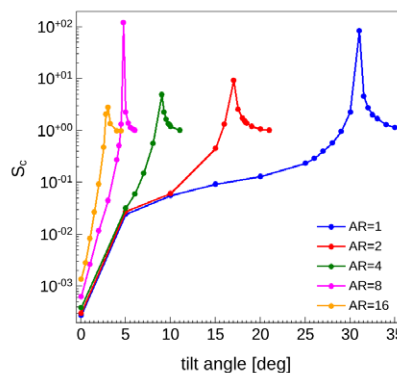


Figure 23: Step coverage (S_c) versus tilt angle for trenches of aspect ratio (AR) 1, 2, 4, 8, and 16 on a rotating wafer.

Figure 24 shows a trench of aspect ratio equal to 1 after PVD of aluminum on a rotating wafer with different tilt angles, namely, 0° , 25° , and 31° . As can be seen in Figure 24(a), when the wafer tilt angle is zero, the step coverage is poor. This is due to the large difference between the flux of incoming particles on the sidewalls and on the bottom of the trench. In fact, if the wafer is not tilted, the trajectories of the incoming particles are almost orthogonal to the bottom and parallel to the sidewalls of the trench. This results in a deposited layer on the bottom much thicker than that on the sidewalls (that is, D_b is much larger than D_{sw}). As shown in Figure 24(b) and (c), the difference between D_b and D_{sw} can be reduced by tilting the wafer. As the tilt angle of the rotating wafer increases, the angle at which particles reach the surface changes, and the incoming particle flux becomes more uniform over the trench, which results in an enhanced step coverage.

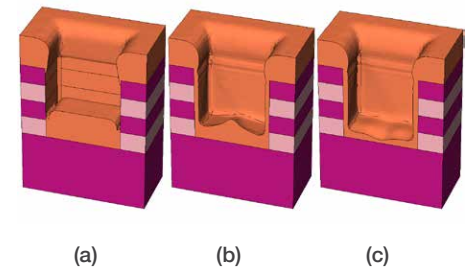


Figure 24: Trench (AR=1) after PVD of aluminum on a rotating wafer with tilt angle (a) 0° , (b) 25° , and (c) 31° . Note the enhanced step coverage for the tilted and rotating wafer.

Sentaurus Device

Driving Forces for High-Field Saturation Mobility Models

The electric field parallel to the current is the physically correct driving force for high-field saturation mobility models³:

$$F = \frac{\vec{E} \cdot \vec{J}_n}{\|\vec{J}_n\|}$$

³We describe the situation for electrons only. Holes are analogous.



Unfortunately, this driving force is susceptible to numerical instabilities for small currents, \vec{j}_n , because the direction of \vec{j}_n is not well defined and fluctuates easily. Therefore the radius of convergence can be very small.

As a more stable alternative, Sentaurus Device uses the gradient of the quasi-Fermi potential:

$$F = \|\nabla\Phi_n\|$$

This `GradQuasiFermi` driving force is the default driving force for drift-diffusion simulations. While it is a stable driving force in most situations, it may still contribute to convergence problems in the case of wide bandgap semiconductors. In this release, a more stable expression for the `GradQuasiFermi` driving force in Sentaurus Device has been developed. The new approach computes a modified `GradQuasiFermi` driving force as an interpolation between the standard `GradQuasiFermi` driving force and the electric field. Alternatively, Sentaurus Device provides a driving force which represents an interpolation between the standard `GradQuasiFermi` driving force and the electric field parallel to the closest semiconductor-insulator interface (`EparallelToInterface`). The electric field parallel to the interface is numerically stable as it does not depend on the direction of the current. It also gives accurate results in those cases where the current flows predominantly parallel to the interface (such as in the channel of MOSFET devices). This new interpolation scheme balances the stability of the `EparallelToInterface` driving force with the higher physical accuracy of the `GradQuasiFermi` driving force.

Incomplete Ionization

In certain semiconductors, dopants may occupy different lattice sites resulting in different activation energies for incomplete ionization. An example is 6H-SiC where the dopant nitrogen can occupy either a hexagonal site h_1 or a cubic site k_1 or k_2 .

This situation can be modeled rigorously by using separate doping species for the different lattice sites. This approach would require the following steps:

- ▶ Introduce new doping species in the file `datexcodes.txt` to describe the concentrations in each lattice site
- ▶ Modify the Sentaurus Process simulation to compute the doping concentrations on the different lattice sites
- ▶ Provide incomplete ionization model parameters for the new doping species

In most cases, however, it is sufficient to specify the average occupation probability of the various lattice sites. For example, if nitrogen is distributed among all three lattice sites in 6H-SiC with equal probability, this can be specified more conveniently in the Sentaurus Device command file:

```
Physics {
  IncompleteIonization (
    Split (
      Doping =
      "NitrogenConcentration"
      Weights = (0.333 0.333
0.334)
    )
  )
}
```

With this new approach it is no longer necessary to modify the file `datexcodes.txt`. Rather the required new doping species are generated by Sentaurus Device on the fly. Similarly, existing Sentaurus Process simulations can be used without any modifications. In this way the physical accuracy of many wide bandgap semiconductor device simulations can be improved with minimal modifications in the simulation setup.

Stress Solver

Mechanical stress has become a major effect in modern semiconductor devices. It is no longer sufficient to consider only a static stress profile during device simulations as the stress within the device may actually change during its operation:

- ▶ Different materials have different thermal expansion coefficients. This thermal mismatch leads to stress changes as a function of the lattice temperature of the device. The influence of thermo-mechanical stress on device performance is investigated in [11] and [12].
- ▶ The electrical degradation of GaN HEMT's is sometimes attributed to the inverse piezoelectric effect, see [13]
- ▶ Gate-dependent polarization charges in GaN HEMT's are investigated in [14]
- ▶ Piezoresistive and piezoelectric materials are the key components of piezoelectronic transistors, see [15]

Beginning with the I-2013.12 release Sentaurus Device can update the stress profile during a simulation in response to changing bias conditions. In this release only thermal mismatch stress as a function of the global device temperature can be modeled.

Sentaurus Device relies on the Sentaurus Process stress solver to recompute stress after the device temperature has changed. For example, Figure 25 shows the device structure of a SiGe HBT (heterojunction bipolar transistor).

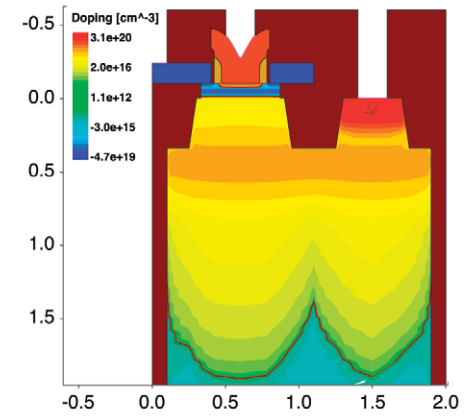


Figure 25: SiGe HBT device structure.



Figure 26 shows the initial profile of the XX component of the stress tensor. We then expose the device to a high current (for example in an ESD event), the device temperature reaches 600K and the stress distribution is recomputed. Figure 27 shows the stress profile at the elevated temperature the stress profile has significantly changed.

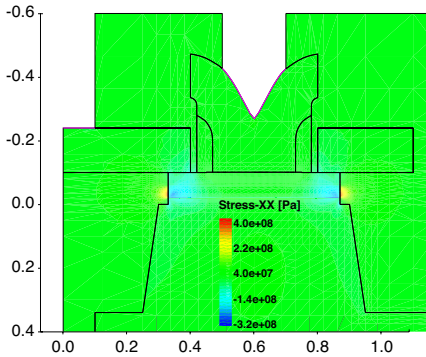


Figure 26: XX component of the Stress Tensor at 300K.

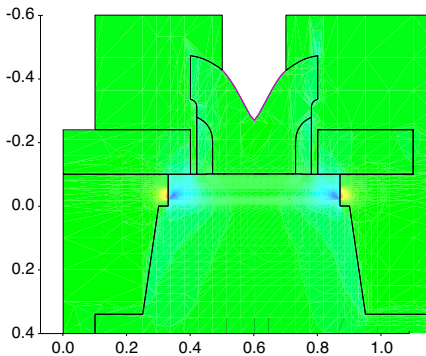


Figure 27: Same as Fig. 26, but after the current induced heating of the device to 600K.

Sentaurus Device updates the stress tensor only on demand when it encounters a Mechanics statement in the Solve section. Therefore the mechanical equations are not solved self-consistently with the device equations. This minimizes overhead and gives the user explicit control over when the mechanical equations are solved. Furthermore, the operation of the Sentaurus Process stress solver can be controlled by providing a corresponding command file.

Improvements for Impedance Field Method

The Impedance Field Method (IFM) is an approach Sentaurus Device uses to model statistical variability. IFM computes the effect of variations in linear response. Thanks to linearization, variations can be handled without solving the nonlinear transport equations repeatedly, which makes the method very fast. Sentaurus Device supports two variants of IFM: Noise-like IFM (nIFM) expresses variations and the response to it by second-order statistical moments. Statistical IFM (sIFM) creates many random samples of the variation, and computes the response for each of them, resulting in an ensemble of response curves.

The new release allows the user to apply the IFM random doping fluctuations (RDF) separately for donors and acceptors. This allows better insight into the origin of random dopant fluctuations in devices. Figure 28 shows the standard deviation of the drain current due to RDF of the acceptors, the donors and the combined effect. The structure itself is shown in the inset. It can be seen that below the threshold voltage the standard deviation of the drain current is dominated by the RDF effect from the channel dopants. Once the channel is fully open, the RDF from the source and drain extension become equally important.

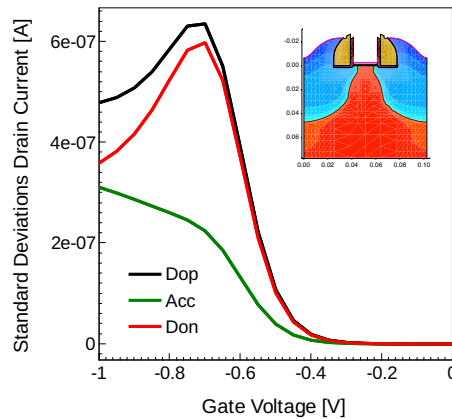


Figure 28: Drain current standard deviation due to random doping fluctuations of acceptors (green), the donors (red), and the all dopants (black) for a 32 nm technology pMOS transistor (shown in the inset).

sIFM now supports the random spatial variation of doping profiles. In contrast to random dopant fluctuations, which are concerned with the discrete nature of dopants and have been available before, doping profiles variations are concerned with the spatial shift of average profiles.

Spatial doping profile variations are most interesting in connection with another new sIFM feature, called "random fields". Random fields are spatial fields of correlated random numbers. These fields can serve as amplitude for various variations: Band edges variations, geometry variations, metal workfunction variations, and doping profile variations. Using the same random field as amplitude for different variations means that these variations are correlated.

The inset of Figure 29 shows a 3D planar nMOS device. Using the random fields, a spatial doping profile variation is imposed to mimic the doping profile variations that would result from line edge roughness (LER) variations of the gate edge (see Figure 29). By selecting independent random fields for the source and drain side the effect of uncorrelated LER is simulated. A spacer-etch process would result in correlated LER on the source and drain-side. This can be

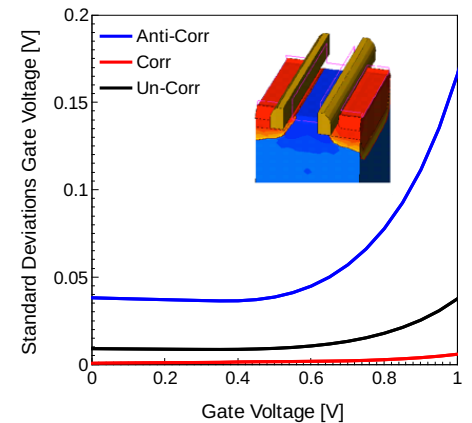


Figure 29: Gate voltage standard deviation due to the line edge roughness effect on the doping profiles assuming that the fluctuations of source and drain sides of the gate edge are anti-correlated (blue), correlated (red) and uncorrelated (back) for 3D planar 32 nm technology nMOS transistor (shown in the inset).



simulated by using a single random field and applying the vectorial shift to the doping profiles. As a “worst-case” scenario one can apply the doping profile shift orthogonal to the doping isolines.

The sIFM now allows any variation to be restricted to a portion of the device by specifying a box. Last but not least, for both nIFM and sIFM, in release I-2013.12 geometric variations of semiconductor/insulator interfaces can work together with the Density Gradient Model, resulting in better accuracy.

Modified Ohmic Boundary Conditions

Ohmic boundary conditions as currently implemented in Sentaurus Device can lead to unphysical results around p-n junctions and hetero-interfaces. The main reason is that this boundary condition imposes strict charge neutrality even at points which are located within depletion regions. Figure 30 shows a typical situation where Ohmic boundary conditions lead to unphysical carrier densities (here an abrupt jump) along the junction connected to the contact.

In this release, Sentaurus Device provides an alternative version of the Ohmic contact boundary condition which does not impose the charge neutrality. In this approach, the equilibrium nonlinear Poisson equation is solved in the beginning of the simulation without considering the Ohmic contact boundary conditions.

The resulting equilibrium electrostatic potential is then used as the boundary condition for the carrier transport equations for the modified Ohmic contacts, instead of the built-in potential which is used in the case of standard Ohmic contacts.

Figure 31 shows the carrier density in a structure described in Figure 30 with standard Ohmic boundary condition used. The non-physical electron density can be seen along the p-n junction with its maximum distortion at the point where the junction touches the Ohmic contact.

Figure 31 displays the same electron density along the junction when the modified Ohmic boundary conditions are used. In this case the solution shows a smooth transition along the junction when we move from bulk towards the contact.

The new feature is supported only for isothermal simulations.

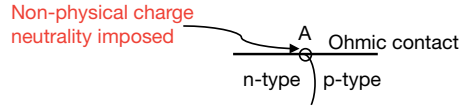


Figure 30: Typical situation where the standard Ohmic contact produces unphysical solution.

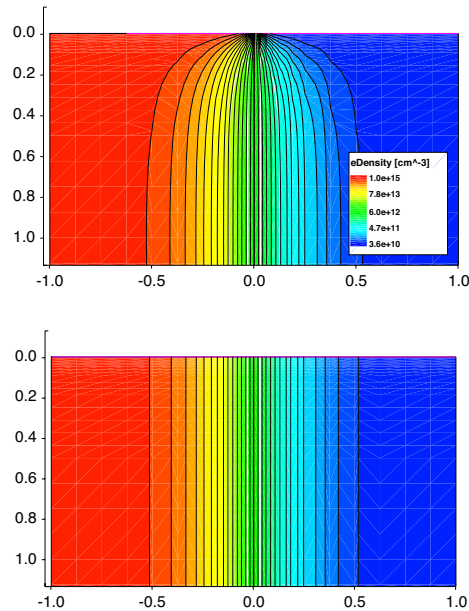


Figure 31: Electron density for a standard (top) and for the new modified Ohmic contact (bottom) on top of a p-n junction.

Hydrogen Transport

In release I-2013.12, the diffusivity and the thermal diffusion term for hydrogen species (hydrogen atoms, hydrogen molecules, and hydrogen ions) can be computed from a physical model interface (PMI). The user-defined models can depend on the magnitude of the electric field, the species concentration, and the lattice temperature.

Stress Models for Silicon-Germanium

The modeling of silicon-germanium and germanium devices requires accounting for the additional L-valleys for electrons, for both, stressed and un-stressed devices. The first Brillion zone of silicon-germanium has four L-valleys in the conduction band which are oriented along the four <111> directions. The relaxed energy of these valleys depends on the germanium molefraction and varies from 1.1 eV above the Δ-valleys for silicon to 0.19 eV below the Δ-valleys for germanium. Additionally the energy of each valley might be changed due to stress. To account for this stress-induced energy change the generalized linear deformation potential model is applied to each L-valley:

$$\delta E = [\Xi_d \hat{1} + \Xi_u \{\vec{e}\vec{e}^T\}]: \hat{\epsilon}$$

where Ξ_d and Ξ_u are user defined deformation potentials, $\hat{\epsilon}$ is the strain tensor, \vec{e} is the unit vector parallel to the k-vector of the L-valley, and the dyadic product is defined as:

$$\hat{a}:\hat{b} = \sum_{i,j} a_{ij}b_{ij}$$

Sentaurus Device provides various models to account for the band structure changes of the silicon-germanium band structure. For typical stress simulations (without using the multi-valley band structure) the DeformationPotential(ekp) and DOS(eMass) models account simultaneously for the Δ-valleys and L-valleys in the band edge and the effective DOS corrections of the conduction band.

Using the multi-valley band structure allows one to account the band structure change more accurately and to consider the carrier density and transport in each valley. For that a new general way to define arbitrary valleys is developed which allows having arbitrary oriented ellipsoidal valleys, the definition of stress and molefraction dependencies, and the setting of non-parabolic and other valley properties. The Multivalley default model parameters are calibrated for silicon-



germanium material and Subband stress-mobility models are developed further to account for arbitrary valleys. The above mentioned models provide the correct physics for modeling stress effects in silicon-germanium devices.

Miscellaneous Mobility Enhancements

Inversion and Accumulation Layer Mobility Model Enhancements

The inversion and accumulation layer mobility model (IALMob) is a model that includes scattering components from the enhanced Lombardi model (Lombardi), the Philips unified mobility model (PhuMob), and also components that account for “two-dimensional” Coulomb impurity scattering in inversion and accumulation layers. Since its original implementation, several enhancements have been made to the model, including support for the auto-orientation framework, support for linear x-mole fraction dependence of model parameters, and support for using IALMob with the ThinLayer model.

For the I-2013.12 release of Sentaurus Device, IALMob has been completely re-implemented resulting in several key benefits:

- ▶ Execution times that are 2X to 3X faster
- ▶ Full mole-fraction support of model parameters (linear, quadratic, and cubic dependencies of both x-mole and y-mole fraction)
- ▶ Additional model dependencies and parameterizations enabling better calibration to experimentally observed results
- ▶ Simplified command and parameter file specification with improved error reporting

New Isotropic Factor Model for Stress-Enhanced Mobility

In general, the presence of mechanical stress in a device results in anisotropic carrier mobility that must be described by a mobility tensor. However, in cases where device current flow is predominantly in a single direction, the mobility enhancement can often be approximated with an isotropic

multiplication factor. Isotropic factor models provide a computationally efficient and robust alternative to the full tensor treatment of stressed enhanced mobility. Previously available isotropic factor models include first- and second-order piezoresistance models and PMI-based models (for example, the MCmob model that is described in the Advanced Calibration for Device Simulation User Guide).

The latest release of Sentaurus Device includes a new isotropic factor model for stress-enhanced mobility called the Effective Stress Model [16]. The mobility enhancement factor dependence on stress enters the model through an effective stress parameter that is calculated from the diagonal components of the stress tensor. An attractive feature of the model is that for a given carrier type, device orientation, and normal electric field, the model predicts the same mobility enhancement for any stress field that gives rise to the same value for the effective stress parameter.

As an example, the left plot of Figure 32 shows (100)/<110> hole mobility enhancement obtained from the Effective Stress Model for various stress conditions. When plotted as a function of the effective stress parameter, these results fall onto a single curve as shown in the right plot.

Stress Factors Applied to Individual Mobility Components

When using an isotropic factor model for stressed-enhanced mobility in previous releases of Sentaurus Device, the calculated enhancement factor was always applied to the total low-field mobility. For better agreement with experimental results, the I-2013.12 release of Sentaurus Device provides an option that makes it possible to apply the calculated enhancement factor to select components of the low-field mobility (for example, only to the acoustic phonon component of the Lombardi model). This is accomplished through mobility component scaling parameters, a_i , that are available for each mobility model that supports this

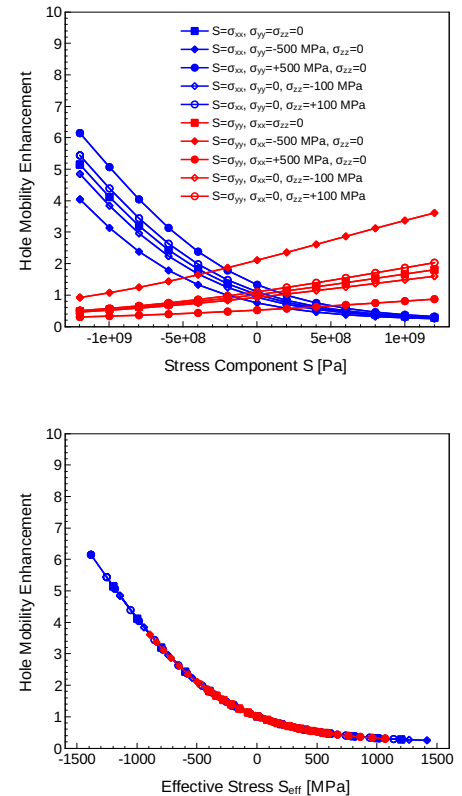


Figure 32: (Left) (100)/<110> hole mobility enhancement obtained with the Effective Stress Model for various stress conditions at a vertical field of $F_{\perp}=0.5$ "MV/cm". (Right) The same results plotted as a function of the effective stress parameter.

feature. For example, specifying $a_{ac}=1$ for the Lombardi model will apply the enhancement factor to the acoustic phonon component of the Lombardi model and specifying $a_{sr}=0$ will ignore the enhancement factor for the surface roughness component.

Mobility models that support this feature include Lombardi, IALMob, InterfaceCharge, Coulomb2D and ThinLayer.

Auto-Orientation for High Field Dependence Parameters

Mobility model parameters accessible in the HighFieldDependence parameter set are now supported with the auto-orientation framework. In particular, this includes all velocity-saturation related parameters for the Canali model, the Transferred Electron Effect model, and the Meinerzhagen-Engl model.

Solver Improvements for Large CIS structures using Periodic Boundary Conditions

Periodic boundary conditions (PBC) are typically used for device structures which are arranged in one- or two-dimensional arrays. A typical application is the simulation of CMOS image sensors (CIS), where PBC emulate the behavior of one cell in an array of cells, while the computational burden is similar to that of a one single cell.

In past releases, the mortar periodic boundary conditions (MPBC) implemented in Sentaurus Device supported the simulation of both one- and two-dimensional arrays.

However, for large 3D device structures, where the use of iterative linear solvers is common, the convergence of MPBC simulations was not sufficiently robust. Use of a direct solver (such as PARDISO) was too time-consuming for large structures.

With this release, it is now possible to use a novel specialized solver for MPBC applications. The so-called Schur solver makes use of ILS and is hence suitable to simulate large 3D device structures. For many case studies where ILS led to convergence problems, the novel Schur solver shows excellent convergence, that is, it improves robustness significantly. The novel solver can be applied both for stationary and transient simulations. The solver supports parallel computations and reaches the efficiency of ILS, in addition to its improved robustness. A comparison of ILS (without periodic boundary conditions, as the MPBC case does not converge) and the Schur solver (using two-fold MPBC) is shown in Table 1, where a transient 3D CIS simulation is performed using 8 threads. The simulation mesh has 120k vertices. It is seen that the parallel performance of the Schur solver is comparable with that of the ILS solver. Table 2 illustrates that the Schur solver improves the performance compared to PARDISO for the same simulation case, now both using MPBC. Both the speed and memory improvements are expected to be even more pronounced for larger structures.

	ILS	SCHUR
MPBC	off	on
Total WC	~1h	~2h
Total tcpu	~6h	~8.5h
#ILS iterations (average)	~80	~70

Table 1: Comparison of performance of ILS (without MPBC) and SCHUR (with MPBC)

	PARDISO	SCHUR
Tcpu per Newton step	~400s	~80 s (80 iterations)
Memory	11.3GB	<7GB
Speedup (8 threads)	~5x	~5x

Table 2: Comparison of performance of PARDISO and SCHUR, both with MPBC, for the same transient simulation case using 8 threads.

Sentaurus Device EMW

In state-of-the-art CMOS image sensors (CIS), designing the pixel is no longer a simple task as it must take into account the complex interactions between the macro lens and the CIS pixel array, all the while maintaining narrower error allowances. When just a simple macro lens is used, the wavefront reaching the micro lens of the CIS pixel can be approximated as a plane wave or a Gaussian beam. As the design of macro lenses becomes more complex so as to meet specific focal lengths and point spread function (PSF) requirements, the resultant wavefront reaching the micro lenses can no longer be described simply by a plane wave or Gaussian beam. Therefore, two basic requirements will help to ensure the successful design and deployment of the modern day CIS: (a) a faster optical solution of each CIS pixel to support optimization, and (b) an interface between the lens design tool and the CIS pixel design tool for more accurate wavefront excitation. Both requirements are fulfilled in the upcoming I-2013.12 release of Sentaurus Device EMW.

To enable the simulation of the entire coupled macro lens and CIS structure, Synopsys has developed a simulation

flow combining CODE V and Sentaurus Device EMW. In this flow, the vectorial electromagnetic field emerging from the macro lens is simulated with CODE V and passed to Sentaurus Device EMW as the input stimulus for the FDTD simulation. CODE V is a widely used lens design tool that supports complex lens design. It uses the BSP (beam synthesis propagation) method to construct a complex vectorial field wavefront that is projected at a designated distance away from the lens. Using the equivalence principle of electromagnetics, the CODE V complex vectorial field wavefront can be automatically formulated into a TFSF (Total Field Scattered Field) excitation wavefront for Sentaurus Device EMW via a simple interface. Sentaurus Device EMW can then accurately compute the light field distribution, scattering and absorption within each CIS pixel. The absorbed photon density is subsequently fed into Sentaurus Device for a full 3D device simulation. As an example, Figure 33 shows the propagated electric fields in the z-y (top row) and z-x (bottom row) plane cuts of the 3D single pixel CIS computed CODE V beam excitation.

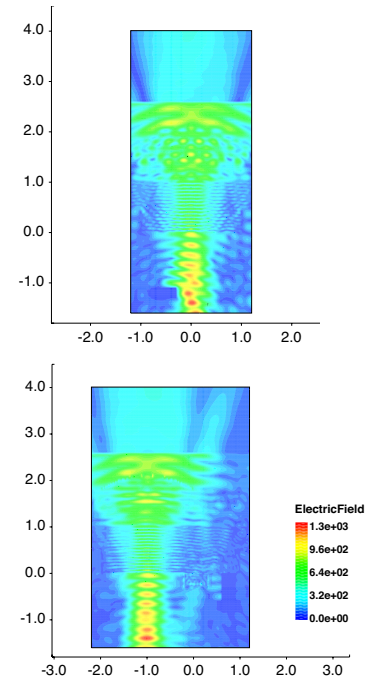


Figure 33: Propagated electric fields in the z-y (left) and z-x (right) plane cuts of the 3D single pixel CIS computed with CODE V beam excitation.



In the area of simulation performance, significant innovations in the MPI (message passing interface) parallelization design of EMW have been implemented, leading to a substantial improvement in the throughput of FDTD simulation of CIS. To showcase the speed improvement between the I-2013.12 and H-2013.03 releases of EMW, we use a generic 1-pixel CIS structure and mesh it into two test cases: (a) 112.6 million cells (Mcells), and (b) 281.3 Mcells. These test cases are typical of 1- and 4-pixels CIS structures, which is indicative of practical cases used in industry. A cluster of machines with the following configuration is used for the speed benchmark tests: each server contains 128GB RAM, 2 sockets with 8 cores per socket and each core running at 2.6 GHz; interconnection between servers uses an 1GB/second switch, and all servers run on Red Hat Enterprise Linux version 5.7. One MPI process is allocated to each socket in the cluster of machines.

A harmonic simulation at a wavelength of 600 nm was used, with a fixed number of time steps so that we can compute the throughput. The throughput is defined as the number of cells processed per second and is an absolute measure of the computational speed of the FDTD algorithm; hence it has been chosen as the speed comparison metric. Figure 34 shows the throughput comparisons of the two test cases. It is evident that the I-2013.12 release consistently outperforms the H-2013.03 release in the MPI parallelization scheme, giving a speedup in the range of 1.4 to 2.8 times. However, it is important to note that parallelization speedup is dependent on many factors such as system architecture and configuration, interconnection switches, OS versions, problem size, decomposition method, etc. Therefore, we urge our users to further test the MPI parallelization in their systems in order to estimate the speed improvement in their own application.

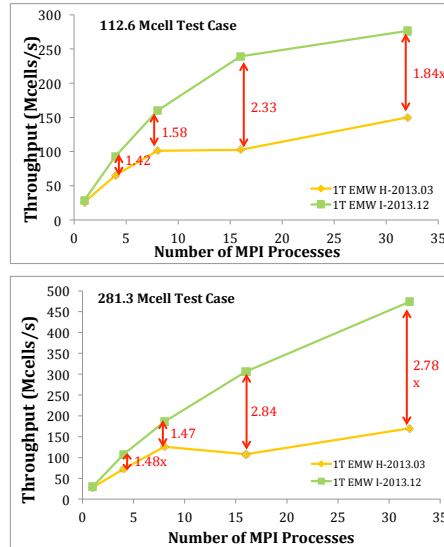


Figure 34: Throughput (Million-cells/second) plotted versus the number of MPI processes for CIS problem sizes of (a) 112.6 Mcells and (b) 281.3 Mcells. The green line denotes the I-2013.12 release of EMW and the orange line denotes the H-2013.03 release. 1T refers to single thread and a pure MPI parallelization scheme is used here.

Sentaurus Device Monte Carlo Monte Carlo Simulation of Germanium Electrons

In addition to multi-gate device architectures, new channel materials are being investigated for further performance enhancement of future CMOS technology nodes. To support this work, the capability to simulate electron transport in relaxed germanium with the Monte Carlo method has been introduced. Compared to electrons in silicon, the L-valleys and the Γ -valley have to be considered. The corresponding scattering model of Jacoboni and Reggiani [17] has been used, where only the values for intravalley acoustic phonon scattering were readjusted to reproduce the measured velocity-field characteristics [18] with the empirical pseudopotential band structure of Rieger/Vogl [19].

Based on band structure and scattering mechanisms for electrons in germanium, the corresponding device performance is assessed via 3D Monte Carlo simulation of the n-type FinFET in Figure 35. A new, more accurate quantum correction scheme is also used to better capture the 2D quantum effects from the fin cross-section [20]. The gate length is 15nm, the fin width is 5.5nm and the fin height is 20nm. The doping levels in the source and drain regions is $3 \times 10^{20} \text{ cm}^{-3}$, in the extension regions $1.5 \times 10^{20} \text{ cm}^{-3}$, and the channel is essentially undoped.

At a supply voltage of 0.8V and a fixed I_{off} of 100 nA/ μm , the I_{dsat} for a Ge channel device reaches 0.95 mA/ μm while a corresponding Si channel device provides 0.52 mA/ μm . Monte Carlo simulation shows a strong Ge performance enhancement because the effective mass in germanium is smaller than in silicon and this strongly enhances quasi-ballistic overshoot effects.

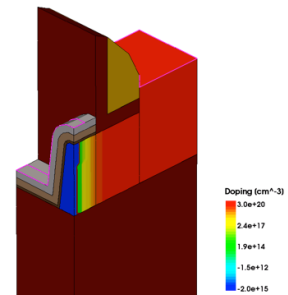


Figure 35: Geometry and doping profile of the MC simulated Ge FinFET with gate length $L=15\text{nm}$, fin height $H=20\text{nm}$, fin width $W=8.5\text{nm}$ at the top and a sidewall angle of 7 degrees.



Subband and Inversion-Layer Mobility Calculator

To treat quantum confinement effects in small FinFETs and nanowires, the solution of the Schrödinger equation in Sentaurus Band Structure has been extended to treat 2D device structures. In addition, new features to compute the thermal injection velocity and the average transport mass have also been enabled.

2D Schrödinger Solver

In this release, the self-consistent solution of the Poisson and Schrödinger equations has been enabled for 2D FinFET and nanowire cross-sections. For NMOS devices, a parabolic Schrödinger solver with built-in stress response and a correction for non-parabolicity can be used. For PMOS devices, a 6-band k-p solver can be enabled. Both approaches enable the treatment of arbitrary strain and device orientation. Device structures generated directly by Sentaurus Process or created as 2D cuts from a 3D device can be used as input.

As an example, Figure 36 shows the self-consistent carrier density in $\langle 110 \rangle$ channel nFinFET and pFinFET cross-sections created by Sentaurus Process using etching and deposition. In this example, the fins are undoped with an approximately 6° sidewall angle and a top width of 6 nm. Using a common mid-gap workfunction, the carrier densities in inversion for both the nFinFET and pFinFET show strong peaks near the top surface with significant density also along each of the sidewalls.

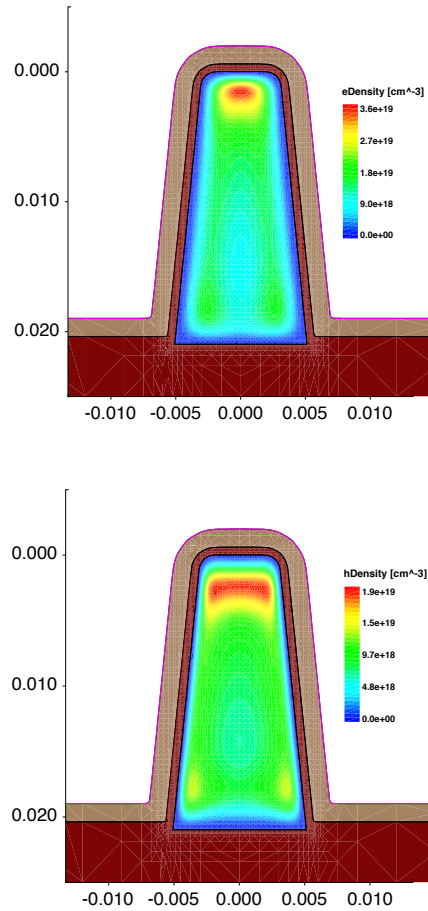


Figure 36: Carrier density in nFinFET (left) and pFinFET(right) cross-sections in inversion computed with the new 2D Schrödinger capability in Sentaurus Band Structure.

Thermal Injection Velocity and Transport Mass

The thermal injection velocity is the average velocity of carriers injected in a particular direction from an equilibrium distribution. In the so-called top-of-the-barrier transport model it represents the ballistic limit of carriers injected into the channel of a MOSFET [21]. It is often used to characterize the ballistic limit of new channel materials and their behavior for different orientation

and strain conditions. In this release, the calculation of the thermal injection velocity from the solution of the Schrödinger equation has been enabled for both 1D and 2D devices. In addition, the average transport mass can also be computed.

As an example, the thermal injection velocities for the device structures shown in Figure 36 are shown in Figure 37 as a function of tensile and compressive uniaxial longitudinal stress for the nFinFET and pFinFET, respectively. For both the nFinFET and pFinFET, the uniaxial stress along $\langle 110 \rangle$ provides a significant increase in the velocity.

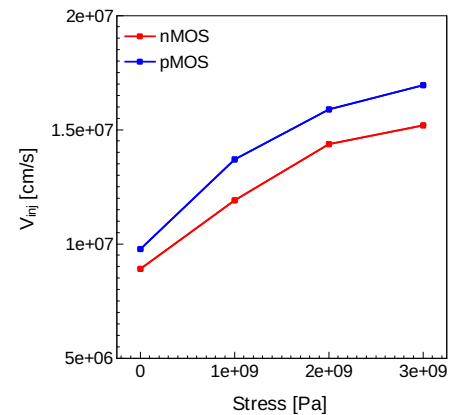


Figure 37: Thermal injection velocity in nMOS and pMOS FinFETs vs. uniaxial stress.

Sentaurus Workbench

Folded Experiments

Having large tables with thousands of experiments makes it difficult to navigate the project and to have a clear overview of the project. Sentaurus Workbench allows the reduction of the table size by folding multiple experiments into a single one. Folding can be applied to split points of the parameterization tree where new experiments appear — these are nodes having two or more children. Folding nodes is very easy: just select the required node and click **Nodes > Fold** in the



popup context menu or the main menu of Sentaurus Workbench. As a result the entire subtree starting with this node will be folded. The following figure shows how the view of the project tree changes after two folding operations: (1) folding nodes 6 and 44; (2) folding nodes 2 and 3.

Figure 38: Original and folded project tree.

Nodes belonging to collapsed experiments represent several nodes and are shown with the specific folded status. These nodes display a range of values of all the nodes behind them. Standard node operations are applicable to folded nodes: preprocessing, running, aborting, cleaning up and visualizing node results. Sentaurus Workbench considers folded node as a multiple-node selection that includes the folded node and all the nodes hidden behind it.

The fold operation is applied from left to right. If the selected node does not have direct children, Sentaurus Workbench tries to fold all the nodes to the right of this node. The configuration of folded nodes is stored with the project and is applied next time the project is loaded in Sentaurus Workbench.

Folding operations is safe since it does not remove any experiments or result files. The fold operation simply hides nodes behind the folded node. Hidden nodes and experiments can be displayed back at any time using the unfold operation. To unfold nodes, select the required folded nodes or nodes to the left and click **Nodes > Unfold** in the popup context menu or the main menu of Sentaurus

Workbench. This operation unfolds the experiments collapsed at that point. If there are folded experiments to the right of this node, the folding will be retained. To unfold all experiments in the current scenario, click **Scenario > Unfold All**. This operation unfolds all the folded experiments and restores the project tree to its original configuration.

Integration with Sentaurus Visual

Sentaurus Workbench continues the support of Sentaurus Visual as the main visualization engine. A deep integration of Sentaurus Workbench and Sentaurus Visual also allows special capabilities that are not available in legacy visualization tools.

Sentaurus Workbench offers the selection of visualization of node output files in a new instance of Sentaurus Visual and in instances of Sentaurus Visual that are already running. Sentaurus Workbench knows the Sentaurus Visual instances that were launched from this current instance of Sentaurus Workbench. The user can choose in which instance of Sentaurus Visual to visualize node output files in a popup dialog box, where already running Sentaurus Visual instances are noted as SWB_1, SWB_2, and so on. To identify the corresponding instance of already Sentaurus Visual, check the title of the main window of Sentaurus Visual, which displays the same identification. This feature makes it easy to compare output files for nodes in different Sentaurus Workbench projects.

For Sentaurus Visual tool steps in the Sentaurus Workbench project simulation flow, the user can chose an enhanced batch mode BatchX which allows Sentaurus Visual to export plot in the batch run. Sentaurus Workbench provides this mode in addition to the traditional Batch and Interactive modes. Sentaurus Workbench also calls Sentaurus Visual for visualizing response surfaces: a surface corresponding to a response surface model (RSM).

Sentaurus Visual

The new version of Sentaurus Visual implements several key features and enhancements to improve its functionality.

Polyline Cuts

A polyline cut is the union of two or more cut lines where the end point of one is the start point of the other. Polyline cuts can be created using the Precision Cut Dialog, or using Tcl commands.

In the GUI, the points that define the polyline can be added either with keyboard entries, by entering the coordinates into textboxes in the dialog box or by clicking the plot with the mouse. The points added are shown with cross marks at the given positions. An example of a plot showing the points while they are being added can be seen in Figure 39.

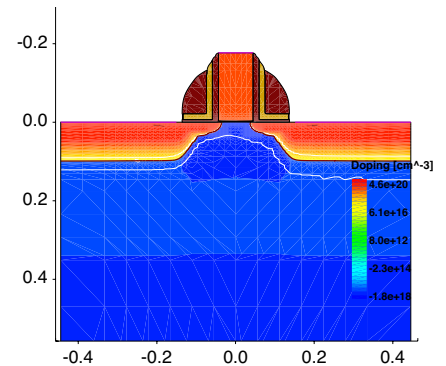


Figure 39: Plot plots the markers while they are being added.

The location of each point can be changed after the cut is created. This can be done by clicking its handles and dragging it to a new position or by modifying the point coordinates in its property panel. This modification will update immediately the resulting XY cut plot.



Cut Along Boundaries

Cuts along boundaries are now possible. This feature enables the extraction of data from the boundary of a group of selected regions that follows a user defined path, defined by two or more points.

In the GUI, users can specify where to initiate and end the cut. The cutline may comprise several segments. Since the cutline segments may not follow exactly the boundary, users can specify which side of the boundary should be plotted.

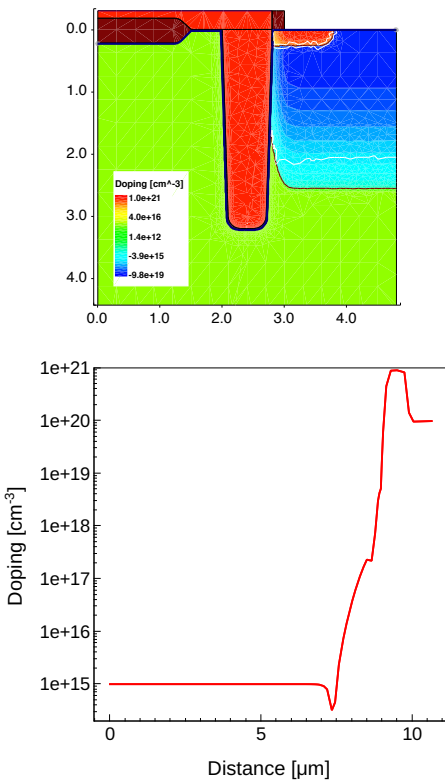


Figure 40: Plot at the left shows the cut along the Silicon boundary. Plot at the right shows the resulting curve of the cut.

New Symbols for KMC

KMC particles can be represented with new symbols, which can be resized and colored. These properties can be set using the Region Properties dialog (CTRL+SHIFT+E). The new shapes for this release are Spheres, Circles, Triangles, Squares and Pentagons.

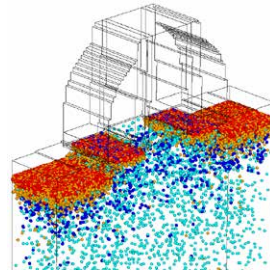


Figure 41: Amorphous pocket particles in silicon shown as small spheres.

User-configurable Contact colors

The new version of Sentaurus Visual adds three ways to define the color for contacts: user defined constant color, selection from a list of colors using round robin logic, and selection by patterns, using a map of colors that accepts wildcards. This new feature enables the coloring of contact regions automatically in these three different ways, thus helping users to better identify the contacts.

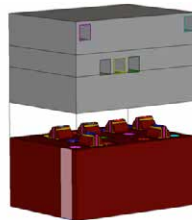


Figure 42: Contacts automatically colored.

2D Projection Plot

It is now possible to create 2D projection plots from 3D plots. The resulting plot is either the maximum or minimum field value projected to one of the planes aligned to the orthogonal axes. The creation of a 2D projection can be done either using the GUI, located in the Tools menu for 3D plots or by Tcl commands. The feature only requires three inputs to calculate the projection: the plane of the projection, the field to display and the function, min or max. Users can also specify the resolution of the projection, which defines the number of points to consider in each axis. Higher resolution will result in a more exact plot but it will take more time to process the data. The projection can be done for the entire structure, in certain regions or materials, or in a user-defined window.

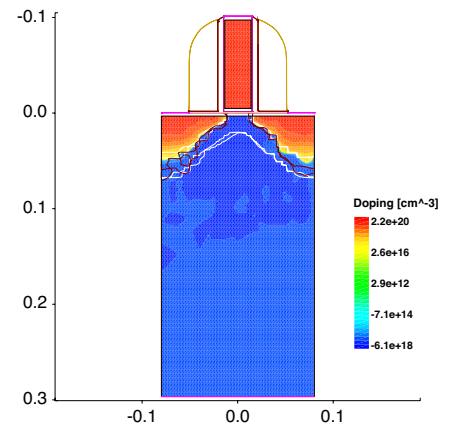
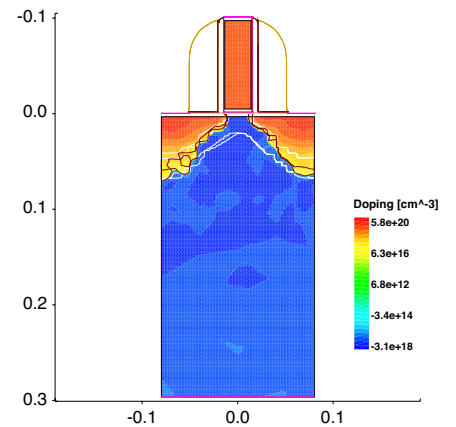
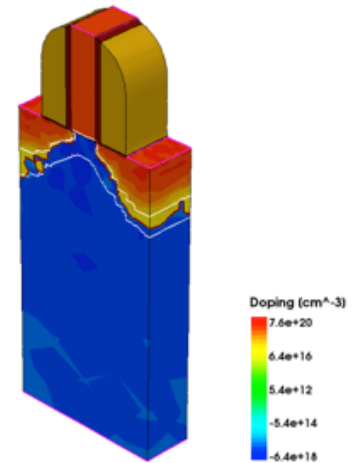


Figure 43: At the left the original plot that wants to be projected. At the middle the projection of the Max values of the Doping. At the right the Min values of the Doping.



Saving Refinement Box to TDR File and Visualizing in Sentaurus Visual

Sentaurus Process provides the functionality of saving refinement boxes to TDR files for users to visualize them in Sentaurus Visual. By default, when a TDR file is loaded into Sentaurus Visual, refinement boxes are not displayed. Displaying the refinement boxes can be activated by checking the item RefinementBox in the Materials list. RefinementBox can be displayed as a bulk shape or just the borders. A list of individual refinement boxes can be found under the Lines/Particles tab.

Figure 44 shows a 2D structure with two overlap refinement boxes. The refinement box is shown in gray borders.

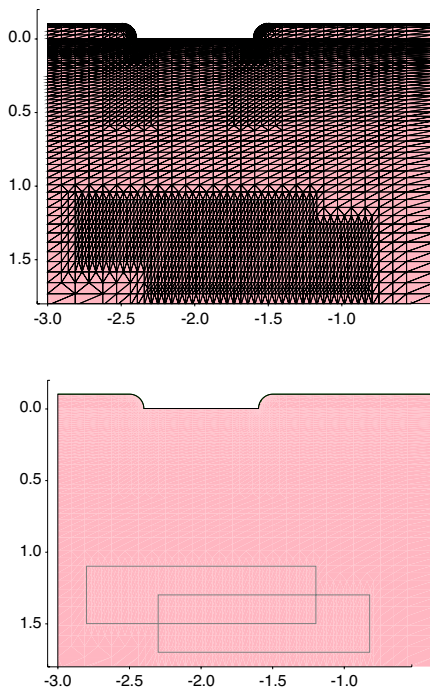


Figure 44: A 2D structure with two overlap refinement boxes. Left: Resulting mesh. Right: Border of the refinement boxes is shown in gray.

Edge Dislocation Visualization

The edge dislocation introduced to the device with the stressdata command can now be saved to TDR file and visualized with Sentaurus Visual. Figure 45 shows an example of visualizing an edge dislocation in a 3D MOSFET with Sentaurus.

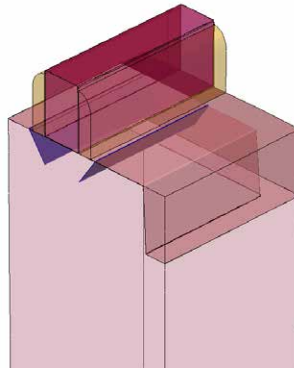


Figure 45: 3D Sentaurus Visual plot of edge dislocations in source and drain areas

RF Support Library

Sentaurus Visual includes a set of specific data post-processing libraries. An example is the Extraction Library for extracting critical parameters from I-V data such as the threshold voltage to the SWB Variables Value section of the Family Tree view. The Impedance Field Method Data Postprocessing Library helps to manage and analyze large amounts of linear current response data. In this release Sentaurus Visual also includes the Two-Port Network RF Extraction Library to extract RF parameters from small-signal data under the assumption that the device or circuit can be represented as a two-port network. As an example, Figure 46 shows the current gain, and various power gains for an InGaAs HEMT. Further, the PhysicalConstants Library was added to give convenient access to the most widely used physical constants that may be needed when writing custom post-processing scripts for Sentaurus Visual.

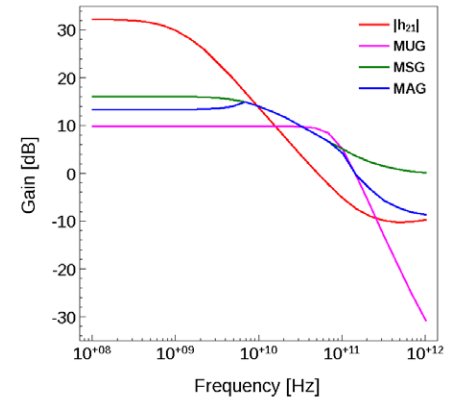


Figure 46: Current gain $|h_{21}|$ and various power gains (Mason's Unilateral Gain MUG, Maximum Stable Gain MSG, and Maximum Available Gain MAG) as a function of frequency for a gate bias of $V_{gs} = 0$ V and a drain bias of $V_{ds} = 1$ V for an InGaAs HEMT with a feedback resistor of $100 \text{ k}\Omega \mu\text{m}$. The RF data is computed using the new Two-Port Network RF Extraction Library in Sentaurus Visualization.

References

- [1] Y. Song, S. Dhar, and L. C. Feldman, "Modified Deal Grove model for the thermal oxidation of silicon carbide", v95, n. 9, Journal of Applied Physics, 2004
- [2] Sanjeev Kumar Gupta and Jamil Akhtar, p.217, Silicon Carbide - Materials, Processing and Applications in Electronic Devices, Intech
- [3] I. Martin-Bragado, N. Zographos, and P. Castrillo, "Atomistic modeling and simulation of arsenic diffusion including mobile arsenic clusters," to be published in Physica Status Solidi.
- [4] S. A. Harrison, T. F. Edgar, and G. S. Hwang, "Interstitial-Mediated Arsenic Clustering in Ultrashallow Junction Formation," Electrochemical and Solid-State Letters, vol. 9, no. 12, pp. G354-G357, 2006.
- [5] H. Riedel and J. R. Rice, "Tensile Cracks in Creeping Solids," *Fracture Mechanics: Twelfth Conference*, ASTM STP 700, American Society for Testing Materials, pp. 112-130, 1980.
- [6] J. L. Bassani and F. A. McClintock, "Creep Relaxation of Stress Around a Crack Tip," *International Journal of Solids and Structures*, vol. 17, pp. 479-492, 1981.
- [7] T. L. Anderson, *Fracture Mechanics*, 3rd Edition, CRC Press, 2005.



- [8] R. A. Schapery, "Correspondence principles and a generalized J integral for large deformation and fracture analysis of viscoelastic media," *International Journal of Fracture*, vol. 25, pp. 195-223, 1984.
- [9] Sentaurus™ *Topography 3D User Guide*, Version I-2013.12, Mountain View, California: Synopsys, Inc., 2013.
- [10] T. Karabacak and T.-M. Lu, "Enhanced step coverage by oblique angle physical vapor deposition," *Journal of Applied Physics*, vol. 97, no. 12, p. 124504, 2005.
- [11] G. Y. Huang and C. M. Tan, "Electrical-Thermal-Stress Coupled-Field Effect in SOI and Partial SOI Lateral Power Diode," *IEEE Transactions on Power Electronics*, vol. 26, no. 6, pp. 1723-1732, June 2011.
- [12] C. M. Tan and G. Huang, "Comparison of SOI and Partial-SOI LDMOSFETs Using Electrical-Thermal-Stress Coupled-Field Effect," *IEEE Transactions on Electron Devices*, vol. 58, no. 10, pp. 3494-3500, October 2011.
- [13] J. Jungwoo and J. Del Alamo, "Mechanisms for Electrical Degradation of GaN High-Electron Mobility Transistors," in *IEDM*, 2006.
- [14] A. Ashok, D. Vasileska, S. M. Goodnick and O. L. Hartin, "Importance of the Gate-Dependent Polarization Charge on the Operation of GaN HEMTs," *IEEE Transactions on Electron Devices*, vol. 56, no. 5, pp. 998-1006, May 2009.
- [15] Y. Zhang, Y. Liu and Z. L. Wang, *Fundamental Theory of Piezotronics*, vol. 23, 2011, pp. 3004-3013.
- [16] A. Kumar, K. Xiu, W. Haensch, R. Robinson, M. Bajaj, J. B. Johnson, S. Furkay and R. Q. Williamson, "A Simple, Unified 3D Stress Model for Device Design in Stress-Enhanced Mobility Technologies," in *International Conference on Simulation of Semiconductor Processes and Devices (SISPAD)*, Denver, CO, USA, September 2012.
- [17] C. Jacoboni and L. Reggiani, "The Monte Carlo method for the solution of charge transport in semiconductors with applications to covalent materials," *Rev. Mod. Phys.*, vol. 55, p. 645 (1983).
- [18] C. Jacoboni, F. Nava and C. Canali, and G. Ottaviani, "Electron drift velocity and diffusivity in germanium," *Phys. Rev. B*, vol. 24, p. 1014 (1981).
- [19] M.M. Rieger and P. Vogl, "Electronic-band parameters in strained Si_{1-x}Ge_x alloys on Si_{1-y}Ge_y substrates," *Phys. Rev. B*, vol. 48, p. 14276 (1993).
- [20] F.M. Butler and L. Smith, "3D Monte Carlo Simulation of FinFET and FDSOI Devices with Accurate Quantum Correction," *J. Comput. Electron.*, to be published.
- [21] A. Rahman et al. "Theory of Ballistic Nanotransistors," *IEEE Transactions on Electron Devices*, vol. 50, no. 9, 1853 (2003).